Materials Characterization 238 (2026) 116669

Contents lists available at ScienceDirect

Materials Characterization

journal homepage: www.elsevier.com/locate/matchar

Heterointerface-induced enhancement of magnetization in $CaFe_2O_4$/$Ca_2Fe_2O_5$ composite fibers

Zhibin Ling [a,1], Feiyu Diao [b,1], Fei Xie [a], Rongsheng Cai [c], Xuyan Xue [a,*], Yiqian Wang [a,*]

[a] College of Physics, Qingdao University, No. 308 Ningxia Road, Qingdao 266071, PR China
[b] College of Textile and Clothing, Qingdao University, No. 308 Ningxia Road, Qingdao 266071, PR China
[c] State Key Laboratory of Solid Lubrication, Lanzhou Institute of Chemical Physics, Chinese Academy of Sciences, Lanzhou 730000, PR China

ARTICLE INFO

Keywords:
Low-dimensional metal oxide
Ferrite
Soft magnetic material
Heterointerface
Saturation magnetization

ABSTRACT

Orthorhombic calcium ferrites, $CaFe_2O_4$ and $Ca_2Fe_2O_5$, have attracted much attention over decades owing to their unique crystal structures and magnetic behaviors. However, their practical application is often hindered by the relatively low magnetization. In this work, a novel strategy, heterointerface engineering, is adopted to enhance their magnetic properties. The $CaFe_2O_4$/$Ca_2Fe_2O_5$ composite fibers are synthesized via electrospinning followed by a high-temperature annealing in air. Magnetic hysteresis loop measurements reveal that the $CaFe_2O_4$/$Ca_2Fe_2O_5$ composite fibers exhibit better magnetic performance compared to their single-phase counterparts, indicating a positive role of the heterointerface in enhancing magnetic properties. Density functional theory calculations further elucidate the underlying mechanism for the enhanced magnetization, which is attributed to the fact that the heterointerface provides a distinct local field environment, thus strengthening the super-exchange interactions between Fe atoms. This work not only presents a facile method for fabricating calcium ferrite heterostructures but also provides fundamental insights into interface-mediated magnetization enhancement, opening avenues for their advanced technological applications.

1. Introduction

Ferrite materials, due to their unique magnetic, electrical, and optical properties, have attracted considerable attention for their vast potential in a wide range of applications, including data storage, sensor technology, catalysis, and biomedical engineering [1,2]. Among the diverse family of ferrites, calcium-based ferrites with an orthorhombic structure, such as $CaFe_2O_4$ and $Ca_2Fe_2O_5$, have garnered particular interest due to their distinctive crystal structures, intriguing magnetic behaviors, and significant potential for multifunctional applications [3–7].

Both $CaFe_2O_4$ ($E_g \sim 1.9$ eV) and $Ca_2Fe_2O_5$ ($E_g = 2.0$–2.2 eV) [8–11] exhibit excellent photocatalytic activities under visible light irradiation and gas sensing performance with promising application prospects. However, they show different magnetic behaviors. $CaFe_2O_4$ exhibits soft magnetic characteristics, such as low coercivity and remanent magnetization, making it suitable for applications in magnetic separation, magnetic hyperthermia, and drug delivery systems [12–14]. $Ca_2Fe_2O_5$ displays more complex magnetic behaviors, which can manifest as antiferromagnetism, weak ferromagnetism, or a spin-glass state [15]. Recent first-principles calculations have revealed that the magnetic properties of $Ca_2Fe_2O_5$ are predominantly governed by short-range magnetic exchange interactions between Fe atoms [16]. Despite multifunctional characteristics of $CaFe_2O_4$ and $Ca_2Fe_2O_5$, their relatively low magnetization has long hindered their practical use in advanced magnetic devices [7,17].

To optimize the physical and chemical performances of $CaFe_2O_4$ and $Ca_2Fe_2O_5$, various strategies have been extensively used, including elemental doping, microscopic morphology regulation, and heterointerface engineering [18–20]. Among these strategies, heterointerface engineering is the most powerful to tailor the physical and chemical properties of ferrites, because the interface between different phases can induce unique electronic structure, charge transfer effect, and magnetic coupling behavior that are not present in the single-phase ferrites [21–23]. Heterointerface engineering has demonstrated a significant potential in diverse applications such as photocatalysis and gas sensor of $CaFe_2O_4$ and $Ca_2Fe_2O_5$. For instance, Luo et al. [24] developed a novel $CaFe_2O_4$/Bi_2O_3 composite, which shows enhanced photocatalytic

* Corresponding authors.
E-mail addresses: xuexy@qdu.edu.cn (X. Xue), yqwang@qdu.edu.cn (Y. Wang).
[1] These authors contribute to this work equally.

https://doi.org/10.1016/j.matchar.2026.116669
Received 12 February 2026; Received in revised form 28 May 2026; Accepted 14 June 2026
Available online 16 June 2026

Table 1
Raw material ratios for different products.

Raw materials			Products
$Ca(acac)_2$ (g)	$Fe(acac)_3$ (g)	Molar ratio	
0.24	0.70	1:2	$CaFe_2O_4$
0.24	0.35	1:1	$Ca_2Fe_2O_5$
0.24	0.52	1:1.5	$CaFe_2O_4/Ca_2Fe_2O_5$

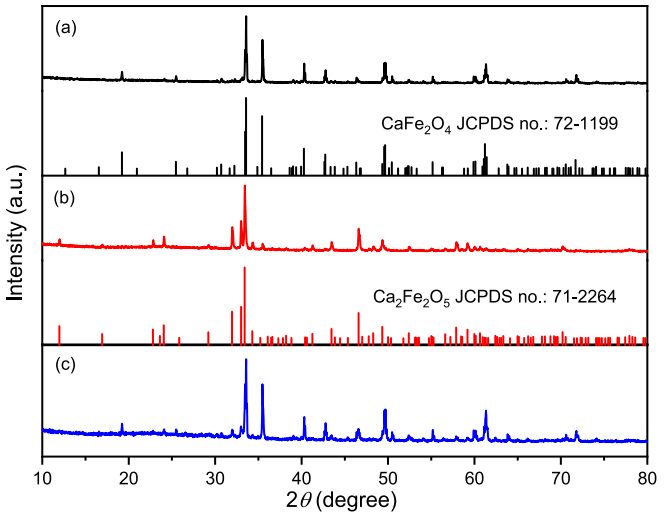

Fig. 1. XRD patterns obtained from CF-12 (a), CF-11 (b), and CF-23 (c).

activity due to the heterojunction structure between Bi_2O_3 and $CaFe_2O_4$. Chang et al. [8] demonstrated that constructing heterointerfaces between $Ca_2Fe_2O_5$ and $CaFe_2O_4$ can effectively modulate the electronic structure and induce an intrinsic electric field at the interface, leading to improved separation of photogenerated charge carriers and enhanced photocatalytic performance. Guo et al. [20] constructed $CaFe_2O_4$/$ZnFe_2O_4$ heterostructures by a hydrothermal method and achieved better gas sensing performance, which was attributed to the improvement of electron-hole separation rate and the decrease of charge transfer resistance. Although heterointerface engineering has achieved remarkable progress in regulating the photocatalytic and gas sensing properties of $CaFe_2O_4$ and $Ca_2Fe_2O_5$, scarce work has been found to enhance their magnetic properties through constructing heterostructure.

In this study, we presented a novel approach to address the critical gap in magnetic enhancement via heterointerface engineering. $CaFe_2O_4$, $Ca_2Fe_2O_5$, and $CaFe_2O_4/Ca_2Fe_2O_5$ submicron fibers were synthesized using electrospinning technique. The composition, microstructure, and magnetic properties of these materials were systematically investigated. First-principles calculations were employed to elucidate the underlying mechanism for the enhancement of magnetic properties at the heterointerface.

2. Experimental

$CaFe_2O_4$, $Ca_2Fe_2O_5$, and $CaFe_2O_4/Ca_2Fe_2O_5$ fibers were fabricated via the electrospinning technique. Calcium acetylacetonate [$Ca(acac)_2$] and iron acetylacetonate [$Fe(acac)_3$] powders, in varying molar ratios (detailed in Table 1), were precisely weighed and placed into a reagent bottle. Subsequently, 0.66 g of polyvinylpyrrolidone was added into the bottle, followed by sequential addition of 3 mL of anhydrous ethanol and 3 mL of glacial acetic acid. The resulting solution was then subjected to continuous stirring for 6 h to ensure formation of a homogeneous and viscous solution. Next, 3–5 mL of this solution was loaded into a syringe for electrospinning.

The electrospinning parameters were optimized as follows [25–27]: a spinning voltage of 16 kV was applied between the needle and the collector at a distance of 15 cm; the injection rate was 0.5 mL/h; the collector of the fibers consisted of a steel plate wrapped with oil paper rotating at 500 rpm; the temperature was 25 °C; the humidity was ~45%. After the electrospinning process was finished, the resulting fiber membrane was carefully removed from the collector drum and dried at 60 °C for 2 h to remove any residual solvents. After drying, the fiber membranes were then annealed at 900 °C for 12 h with a heating rate of 5 °C/min in an air atmosphere. The final products were obtained after the annealing process. The obtained fiber membranes with Ca:Fe ratios of 1:1, 1:2 and 1:1.5 were named as CF-11, CF-12 and CF-23, respectively.

The crystal structures of three products were analyzed by an X-ray diffractometer (XRD, Bruker D8 Advance) with Cu-K_α radiation (λ = 1.5406 Å). The morphology of the products was examined using a field-emission SEM (FE-SEM, Sigma 500) operating at 15 kV. X-ray photoelectron spectroscopy (XPS) spectra were acquired using a Thermo Scientific K-Alpha$^+$ XPS spectrometer equipped with an Al K_α X-ray source. Bright-field (BF) images, high-resolution transmission electron microscopy (HRTEM) images and selected-area electron diffraction (SAED) patterns were obtained using a field-emission transmission electron microscope (TEM, JEOL JEM2100F) operating at 200 kV. The elemental mapping of the fibers was carried out using energy dispersive X-ray spectrometer (EDS, Oxford INCAx-sight 6427). The high-angle annular dark field (HAADF) imaging was performed using a probe-corrected Thermo Scientific Spectra 300 (S)TEM with an accelerating voltage of 300 kV. The magnetization versus magnetic field hysteresis loops were measured by a vibrating sample magnetometer (VSM) equipped on a physical properties measurement system (PPMS, Quantum Design) at room temperature.

Spin-polarized electronic structure calculations were performed using the plane-wave basis set method, as implemented in the Vienna Ab initio Simulation Package (VASP) [28]. The projector augmented wave pseudopotential (PAW) was employed to describe the interactions between ions and core electrons. The exchange and correlation effects were described using the Perdew-Burke-Ernzerhof (PBE) within the framework of generalized gradient approximation (GGA) [29]. The cutoff energy for the truncation of plane-wave bias was set to be 520 eV, and the accuracy of the electron self-consistent field was set to be 10^{-6} eV. A Brillouin zone *k*-point sampling with a resolution of $2\pi \times 0.05$ Å^{-1} was used. The convergence criterion is 0.01 eV/Å for the forces acting on the atoms. The spin-polarized calculations for collinear magnetism were performed self-consistently.

3. Results and discussion

To investigate the crystal structure of the as-synthesized products, XRD analysis was conducted, as shown in Fig. 1. The XRD patterns reveal that all three products exhibit good crystallinity. Fig. 1(a) shows the XRD pattern obtained from the product of CF-12, which can be indexed using orthorhombic $CaFe_2O_4$ (JCPDS #72–1199). The diffraction peaks at 19.2°, 33.5°, 33.6°, 35.4°, 40.3°, 42.7°, 49.5°, 49.7°, and 61.2° correspond to the (120), (040), (320), (121), (131), (311), (241), (401), and (441) crystal planes of orthorhombic $CaFe_2O_4$, respectively. Therefore, the obtained product named as CF-12 can be identified as $CaFe_2O_4$. Fig. 1(b) shows the XRD pattern of CF-11, where the diffraction peaks align well with the standard pattern of orthorhombic $Ca_2Fe_2O_5$ (JCPDS #71–2264). The diffraction peaks at 24.0°, 31.9°, 33.0°, 33.4°, 46.6°, 49.3°, and 57.9° correspond to the (031), (002), (200), (141), (202), (062), and (143) crystal planes of orthorhombic $Ca_2Fe_2O_5$, indicating the formation of $Ca_2Fe_2O_5$. Fig. 1(c) shows the XRD pattern of CF-23, revealing coexistence of both CF-12 and CF-11, which suggests the formation of $CaFe_2O_4$ and $Ca_2Fe_2O_5$ in the CF-23. Furthermore, quantitative analysis of Fig. 1(c) indicates that the molar ratio of $CaFe_2O_4$ to $Ca_2Fe_2O_5$ in CF23 is approximately 2:1. Accordingly, the overall Ca to Fe atomic ratio in the composite is calculated to be

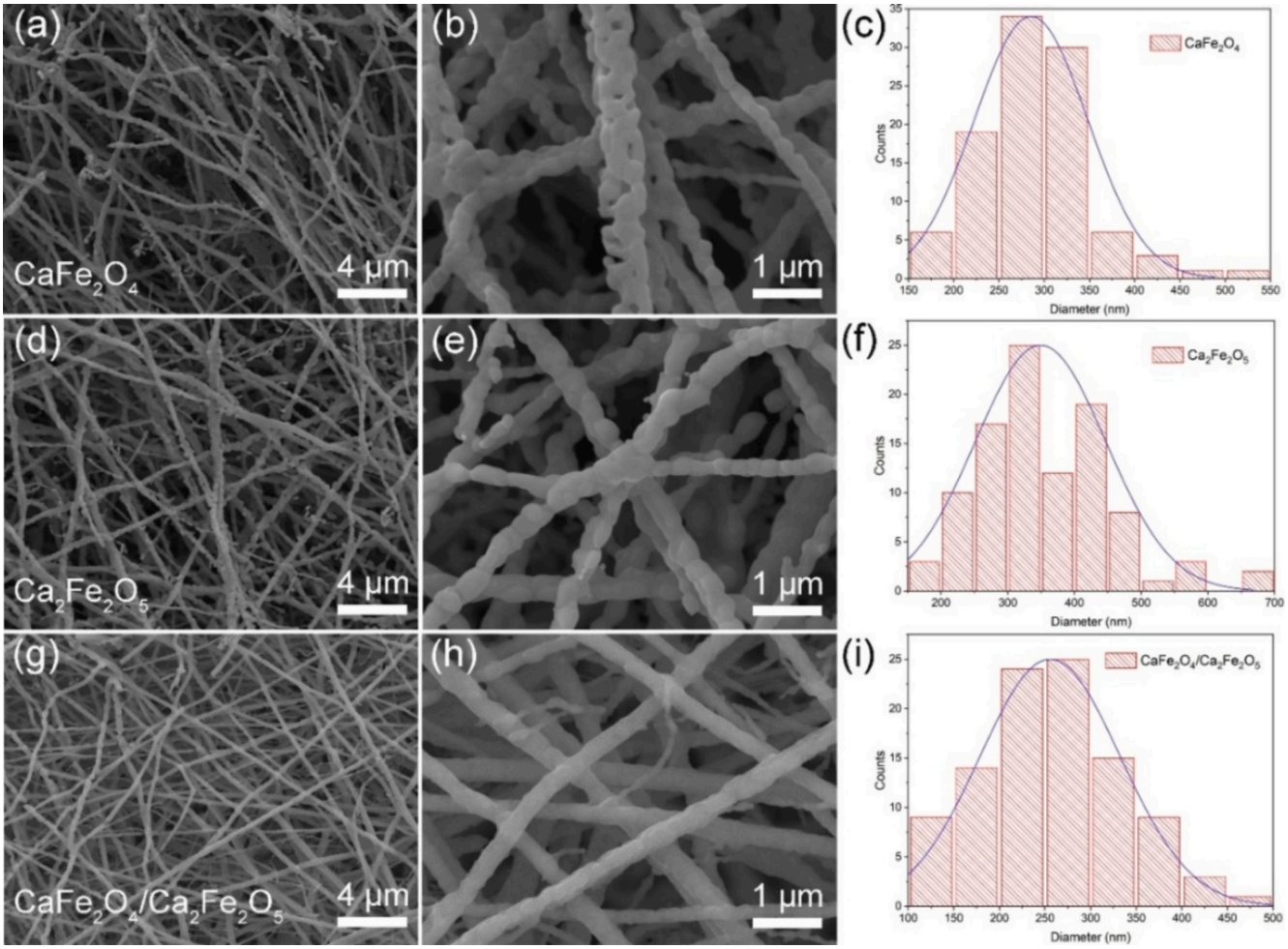

Fig. 2. SEM images and diameter distributions of $CaFe_2O_4$ (a, b, c), $Ca_2Fe_2O_5$ (d, e, f) and $CaFe_2O_4/Ca_2Fe_2O_5$ (g, h, i) submicron fibers.

1:1.5, which aligns precisely with the molar ratio of the precursors used in the synthesis process. This demonstrates that the phase composition can be effectively controlled by adjusting the molar ratio of precursors [30–35].

SEM examination was conducted to characterize the morphology of the three products, as displayed in Fig. 2. Fig. 2(a) presents a low-magnification SEM image of CF-12, showing that the diameters of the fibers range from 200 nm to 400 nm. Fig. 2(b) is an enlarged SEM image, revealing that these fibers are composed of numerous small particles and have a porous surface morphology. In comparison, the $Ca_2Fe_2O_5$ fibers (Fig. 2(d) and (e)) exhibit a more uniform length distribution and their diameters range from 200 nm to 500 nm. At higher magnification, we can see that the $Ca_2Fe_2O_5$ fibers are composed of numerous particles with relatively larger size and much less surface pores than those observed in $CaFe_2O_4$. The differences in morphology are mainly due to the varying amounts of organic ligands and the phase structures. The higher amounts of organic ligands in the $CaFe_2O_4$ precursor releases more gas during annealing, creating a porous surface. For $Ca_2Fe_2O_5$, the lower amounts of organic ligands result in less gas evolution, allowing grains to grow larger and form a denser surface. Fig. 2(g) shows the low-magnification SEM image of the CF23, which displays relatively uniform fibers with diameters ranging from 150 to 400 nm. The magnified image in Fig. 2(h) further confirms that the composite fibers consist of fine grains. Notably, the surface of the $CaFe_2O_4/Ca_2Fe_2O_5$ composite fibers appears smoother and more compact compared to the single-phase fibers. This is because the coexistence of $CaFe_2O_4$ and $Ca_2Fe_2O_5$ phases restricts grain growth by mutually limiting crystallization expansion. The resulting small, uniform grains pack densely, forming a continuous surface. This observation implies an enhanced interfacial interaction between the constituent particles and suggests the potential formation of a heterojunction structure between $CaFe_2O_4$ and $Ca_2Fe_2O_5$.

To investigate the surface elemental valence states of $CaFe_2O_4$, $Ca_2Fe_2O_5$, and $CaFe_2O_4/Ca_2Fe_2O_5$ fibers, XPS examination was conducted, as presented in Fig. 3. Figs. 3(a), (b), and (c) depict the high-resolution XPS spectra of the Ca 2*p*, Fe 2*p*, and O 1 *s* in the $CaFe_2O_4$ fibers, respectively. In Fig. 3(a), the peaks at 350.89 eV and 347.3 eV correspond to the $2p_{1/2}$ and $2p_{3/2}$ of Ca^{2+}, indicating that the valence state of Ca in the fibers is +2 [36]. In Fig. 3(b), the peaks at 724.3 eV and 710.7 eV correspond to the $2p_{1/2}$ and $2p_{3/2}$ of Fe^{3+}, with satellite peaks at 718 eV and 733 eV, confirming that the valence state of Fe in the product is +3 [20]. In Fig. 3(c), peaks at 531.5 eV and 529.9 eV correspond to surface-adsorbed oxygen and lattice oxygen within the fibers, respectively [30]. Figs. 3(d), (e), and (f) show the high-resolution XPS spectra of the Ca 2*p*, Fe 2*p*, and O 1 *s* of $Ca_2Fe_2O_5$ fibers, respectively. In Fig. 3(d), the peaks at 351.31 eV and 347.64 eV correspond to the $2p_{1/2}$ and $2p_{3/2}$ of Ca^{2+}, indicating a + 2 valence state for Ca [20]. In Fig. 3(e), the peaks at 724.3 eV and 710.7 eV correspond to the $2p_{1/2}$ and $2p_{3/2}$ of Fe^{3+}, with satellite peaks at 718 eV and 733 eV, indicating that the valence state of Fe in $Ca_2Fe_2O_5$ is +3. In Fig. 3(f), the peaks at 531.5 eV and 529.9 eV correspond to surface-adsorbed oxygen and lattice oxygen, respectively. Compared to $CaFe_2O_4$ fibers, the intensity of the surface-adsorbed oxygen peak in $Ca_2Fe_2O_5$ fibers is significantly reduced. This phenomenon can be attributed to the porous structure of $CaFe_2O_4$ submicron fibers. Figs. 3(g), (h), and (i) present the XPS spectra of the Ca 2*p*, Fe 2*p*, and O 1 *s* of the $CaFe_2O_4/Ca_2Fe_2O_5$ composite fibers, respectively. It can be seen that the main peaks positions of Ca 2*p*, Fe 2*p*, and O 1 *s* in

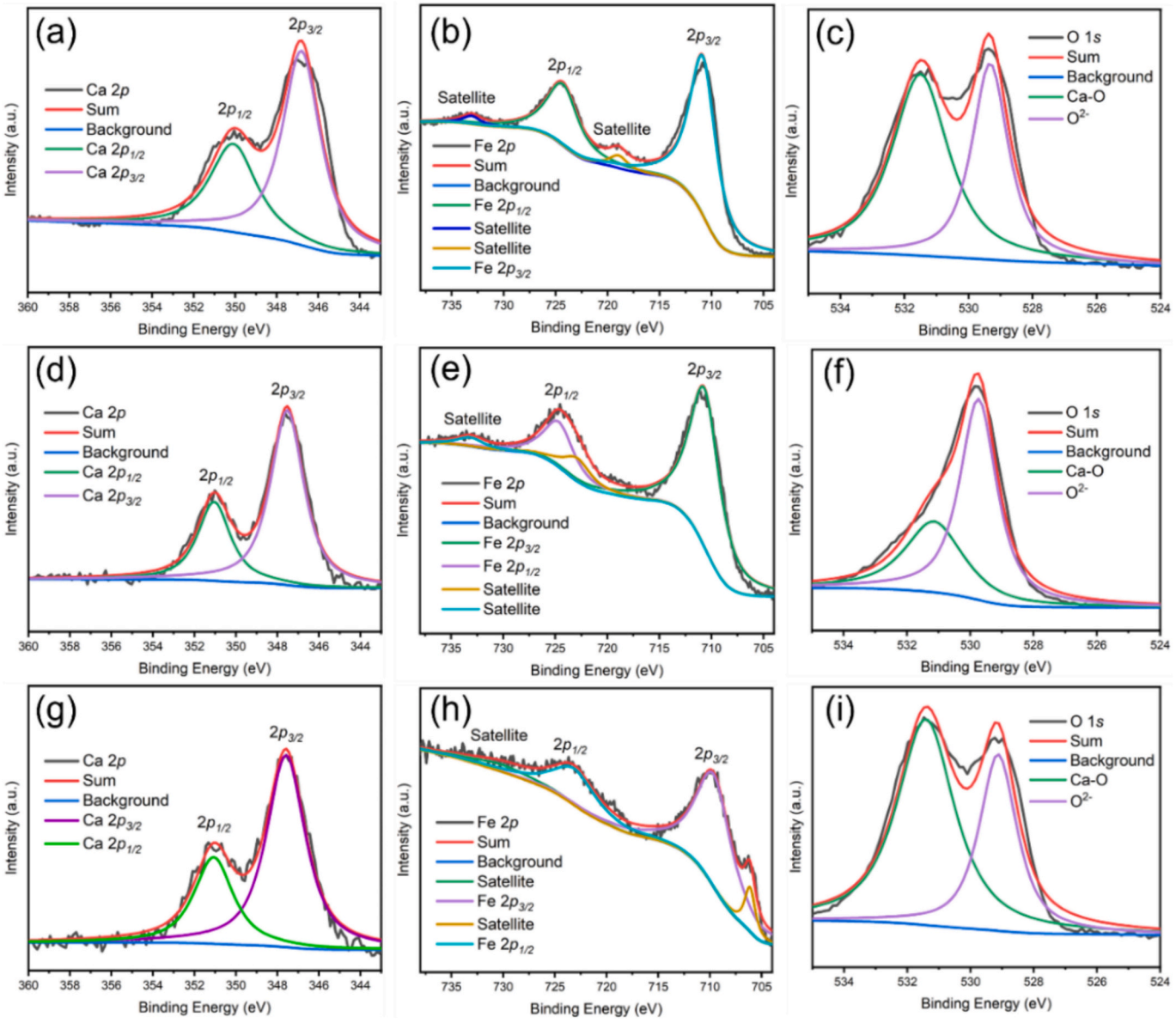

Fig. 3. XPS spectra of Ca, Fe, and O in $CaFe_2O_4$ (a, b, c), $Ca_2Fe_2O_5$ (d, e, f), and $CaFe_2O_4/Ca_2Fe_2O_5$ (g, h, i) submicron fibers.

the $CaFe_2O_4/Ca_2Fe_2O_5$ composite fibers remain the same as those in the $CaFe_2O_4$ and $Ca_2Fe_2O_5$ fibers. However, different from the spectra of $CaFe_2O_4$ and $Ca_2Fe_2O_5$ fibers, a new satellite peak appears at 706 eV in the Fe 2*p* spectrum of the composite fibers, indicating a change in the electronic structure of some Fe atoms in the composite fibers. This phenomenon is likely induced by the formation of a $CaFe_2O_4/Ca_2Fe_2O_5$ heterostructure interface within the composite fibers.

To further investigate the microstructure of $CaFe_2O_4$, $Ca_2Fe_2O_5$, and $CaFe_2O_4/Ca_2Fe_2O_5$ fibers, extensive TEM examinations were performed. Fig. 4(a) shows a BF TEM image of $CaFe_2O_4$ fibers, revealing that the fibers are composed of small particles, consistent with the SEM observations. The inset displays the polycrystalline diffraction pattern, which corresponds to the (040), (400), (260), and (540) planes of the orthorhombic $CaFe_2O_4$. Fig. 4(b) presents the SAED pattern of the grains enclosed by a white rectangle in Fig. 4(a), which can be indexed as the [001] zone axis of orthorhombic $CaFe_2O_4$. Fig. 4(c) displays the corresponding HRTEM image. Fig. 4(d) is an enlarged view of the region enclosed by a white rectangle in Fig. 4(c), where the interplanar spacings are measured to be 2.67 Å and 2.68 Å, corresponding to the (320) and (040) planes of the orthorhombic $CaFe_2O_4$, respectively. From the above, it is concluded that the $CaFe_2O_4$ fibers are composed of numerous $CaFe_2O_4$ nanoparticles.

Fig. 5(a) shows a BF TEM image of $Ca_2Fe_2O_5$ fibers, indicating that the $Ca_2Fe_2O_5$ fibers are also composed of small particles, consistent with the SEM observations. The polycrystalline diffraction pattern in inset of Fig. 5(a) can be indexed from inside to outside with (002), (222), (113) and (004) planes of orthorhombic $Ca_2Fe_2O_5$. Fig. 5(b) presents the SAED pattern of the grains enclosed by a white rectangle in Fig. 5(a), which can be indexed as the $[1\bar{1}0]$ zone axis of the orthorhombic $Ca_2Fe_2O_5$. Fig. 5(c) displays the corresponding HRTEM image. Fig. 5(d) is an enlarged view of the region enclosed by a white rectangle in Fig. 5(c), where the interplanar spacings are measured to be 2.80 Å and 2.55 Å, corresponding to the (002) and (220) planes of the orthorhombic $Ca_2Fe_2O_5$, respectively. Based on the above analysis, it can be concluded that the $Ca_2Fe_2O_5$ fibers are composed of numerous $Ca_2Fe_2O_5$ nanoparticles.

Fig. 6(a) shows a BF TEM image of $CaFe_2O_4/Ca_2Fe_2O_5$ composite fibers, revealing that the fibers are composed of numerous particles. Compared to $CaFe_2O_4$ and $Ca_2Fe_2O_5$ fibers, the nanoparticles in the $CaFe_2O_4/Ca_2Fe_2O_5$ fibers are smaller in size and more densely packed.

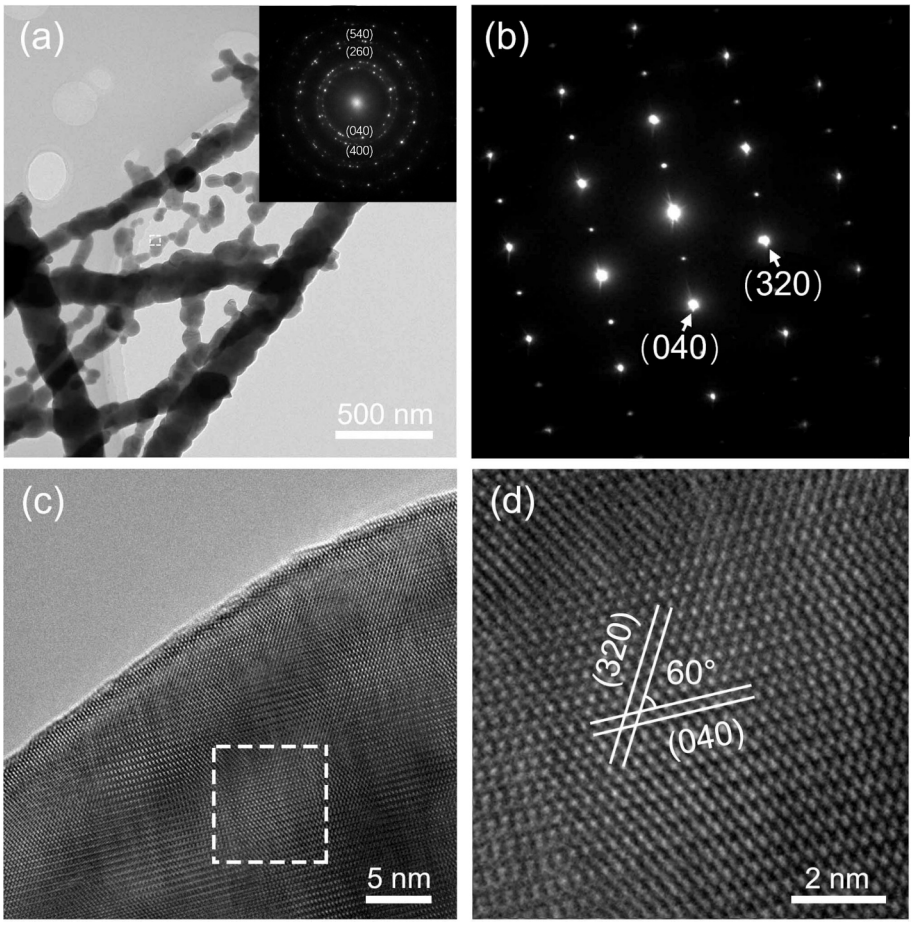

Fig. 4. TEM images of $CaFe_2O_4$ submicron fibers. (a) Bright-field image (inset showing polycrystalline diffraction pattern), (b) SAED pattern of the grains within the white rectangular region in (a), (c) HRTEM image of a localized region in a single grain, (d) Enlarged view of the region enclosed by a rectangle in (c).

Fig. 6(b) is an enlarged image of the region enclosed by a white rectangle in Fig. 6(a). Figs. 6(c), (d), and (e) display the SAED patterns of the three grains labeled I, II, and III in Fig. 6(b). The patterns in Figs. 6(c) and (d) can be indexed as the $[13\bar{3}]$ zone axis of the orthorhombic $CaFe_2O_4$, while the pattern in Fig. 6(e) can be indexed as the $[1\bar{2}1]$ zone axis of the orthorhombic $Ca_2Fe_2O_5$.

Figs. 7(a-c) present the HRTEM images of the three grains. Figs. 7(d), (e), and (f) are the enlarged HRTEM images of grains I, II, and III, respectively. In Fig. 7(d), the interplanar spacings are measured to be 2.91 Å and 2.96 Å, corresponding to the (011) and (301) planes of $CaFe_2O_4$. In Fig. 7(e), the two crystal planes can be indexed as the (011) and (301) planes of $CaFe_2O_4$. In Fig. 7(f), the interplanar spacings are 3.89 Å and 3.76 Å, consistent with the $(\bar{1}01)$ and (111) planes of $Ca_2Fe_2O_5$. These results confirm that grains I, II, and III are $CaFe_2O_4$, $CaFe_2O_4$, and $Ca_2Fe_2O_5$ nanocrystals, respectively. Further detailed observation reveals that the grain boundaries of grains I, II, and III are tightly interconnected, leading to the formation of $CaFe_2O_4/Ca_2Fe_2O_5$ heterostructure interfaces between grain I and grain III, grain II and grain III. Fig. 8 shows the EDS elemental mappings of three grains, indicating the uniform distribution of Ca, Fe, and O within the fibers. No elemental signals other than Ca, Fe, and O are detected across the observed region, confirming that the grains contain only these three elements.

The heterostructure interface of $CaFe_2O_4/Ca_2Fe_2O_5$ was further investigated using STEM, as shown in Fig. 9. Fig. 9(a) shows a HAADF image of the nanocrystal interface in $CaFe_2O_4/Ca_2Fe_2O_5$ composite fibers. For ease of description and analysis, the two grains in Fig. 9(a) are labeled as IV and V, and the interface between them is designated as VI. Figs. 9(b) and (c) are the enlarged HAADF images of grain IV and V, respectively. The interplanar spacing in grain IV is 2.96 Å, consistent with the (301) plane of $CaFe_2O_4$ along the $[13\bar{3}]$ zone axis. In Fig. 9(c), the interplanar spacing in grain V is 3.89 Å, matching the (101) plane of $Ca_2Fe_2O_5$ along the [010] zone axis. Fig. 9(d) is an enlarged HAADF image of VI, clearly showing that a stable heterostructure interface is formed between $CaFe_2O_4$ and $Ca_2Fe_2O_5$. The inset in Fig. 9(d) illustrates a schematic diagram of the atomic structures for $CaFe_2O_4$ and $Ca_2Fe_2O_5$ along the $[13\bar{3}]$ and [010] zone axes, respectively. These HAADF images provide direct evidence of the existence of heterostructure interface between $CaFe_2O_4$ and $Ca_2Fe_2O_5$ crystal grains in the $CaFe_2O_4/Ca_2Fe_2O_5$ composite fibers. These heterostructure interfaces in the composite fibers are expected to have great influence on their magnetic properties.

To investigate the influence of heterostructure interface on the magnetic properties, the hysteresis loops of $CaFe_2O_4$, $Ca_2Fe_2O_5$ and $CaFe_2O_4/Ca_2Fe_2O_5$ fibers were measured, as shown in Fig. 10. From Fig. 10(a), it can be seen that the loops of $CaFe_2O_4$, $Ca_2Fe_2O_5$, and $CaFe_2O_4/Ca_2Fe_2O_5$ fibers exhibit typical soft magnetic characteristics. All the three ferrite fibers easily reach magnetic saturation (M_s) under an external magnetic field. Further observation reveals that the M_s of $CaFe_2O_4/Ca_2Fe_2O_5$ composite fibers is significantly higher than that of $CaFe_2O_4$ and $Ca_2Fe_2O_5$. Fig. 10(b) displays a magnified view near the zero-field region of Fig. 10(a), which clearly shows that all three materials exhibit low coercive forces (H_c), approximately 70 Oe. The remnant magnetism (M_r) of both $CaFe_2O_4$ and $Ca_2Fe_2O_5$ is similar, approximately at 0.05 emu/g. Whereas the $CaFe_2O_4/Ca_2Fe_2O_5$ composite fibers with a heterostructure interface exhibit a significantly higher M_r of 0.1 emu/g. In addition, all three submicron fibers reach M_s

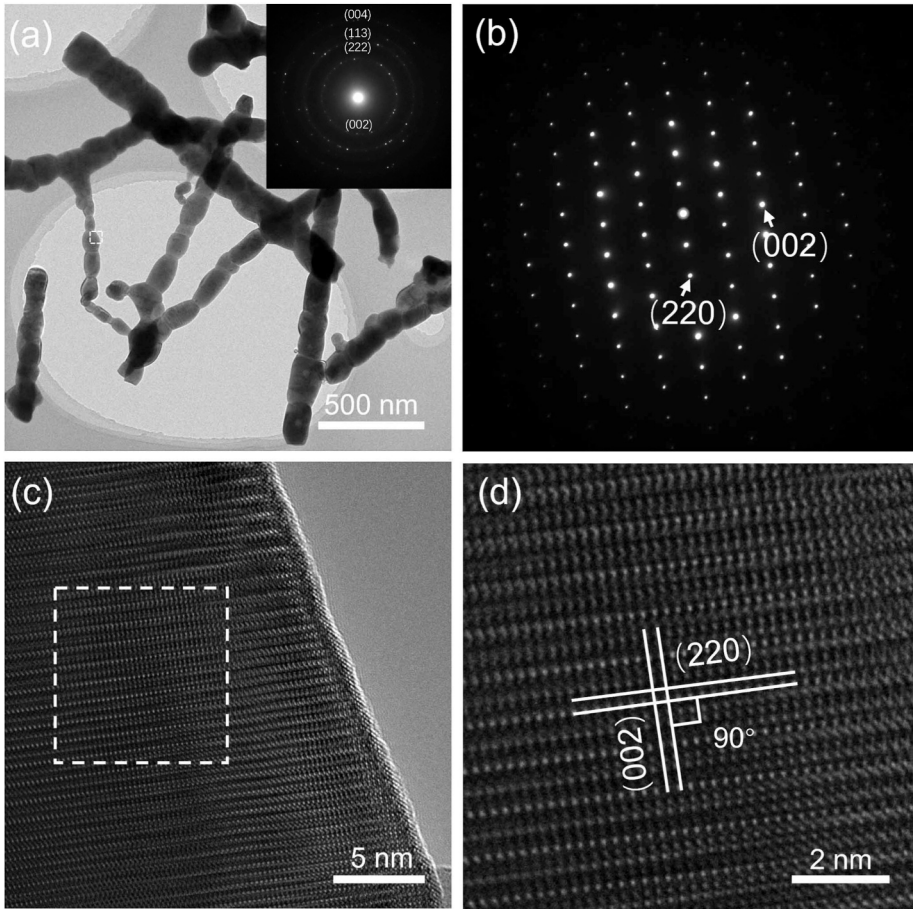

Fig. 5. TEM images of $Ca_2Fe_2O_5$ submicron fibers. (a) Bright-field image (inset showing polycrystalline diffraction pattern), (b) SAED pattern of the grains within the region enclosed by a white rectangle in (a), (c) HRTEM image of a localized region in a single grain, (d) Enlarged view of the region enclosed by a rectangle in (c).

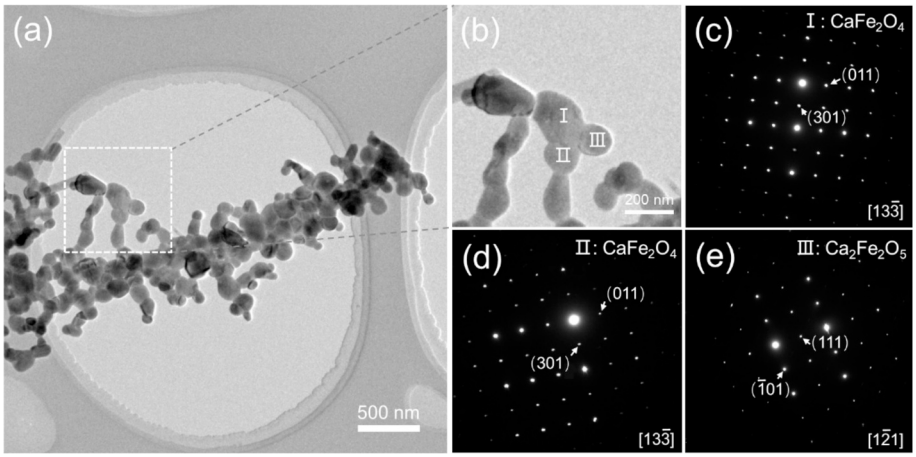

Fig. 6. TEM images of $CaFe_2O_4/Ca_2Fe_2O_5$ submicron composite fibers. (a) Bright-field image, (b) Enlarged view of the region enclosed by a white rectangle in (a), SAED patterns obtained from grain I (c), grain II (d), and grain III (e).

at an external magnetic field of 1000 Oe. The M_s of the $CaFe_2O_4/Ca_2Fe_2O_5$ composite fibers is approximately 0.38 emu/g, notably higher than that of $CaFe_2O_4$ and $Ca_2Fe_2O_5$ (~ 0.19 emu/g). These experimental results indicate that the introduction of a heterostructure interface has a slight influence on the H_c but significantly enhances the M_r and M_s, thereby improving the overall magnetic performance of the as prepared ferrites. Furthermore, all the three ferrite fibers exhibit super-paramagnetic behavior [37], which can be attributed to the small grain sizes within the fibers [38] and the non-magnetic nature of Ca atoms [39].

While the magnetization levels achieved here remain lower than those of conventional soft magnetic materials, the demonstrated enhancement via heterointerface engineering provides a viable route for tailoring magnetic properties, and the resulting enhanced magnetization may be sufficient for applications such as magnetically recoverable catalysts and biosensing platforms [40–43] where multifunctionality is

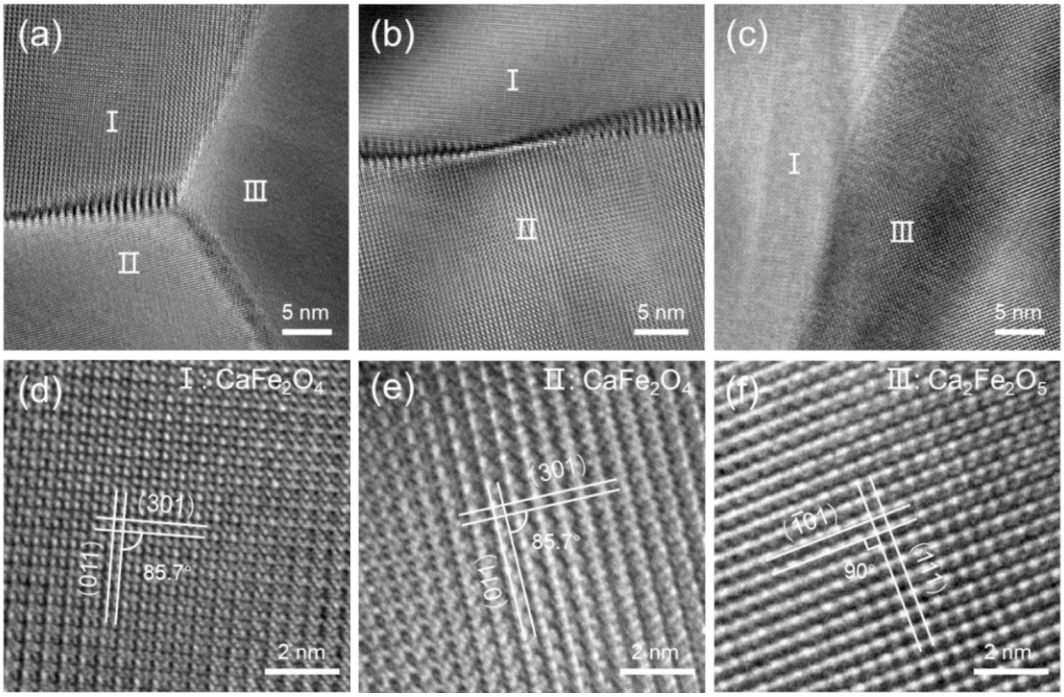

Fig. 7. (a-c) HRTEM images of $CaFe_2O_4/Ca_2Fe_2O_5$ composite fibers. Enlarged HRTEM images for grain I (d), grain II (e), and grain III (f).

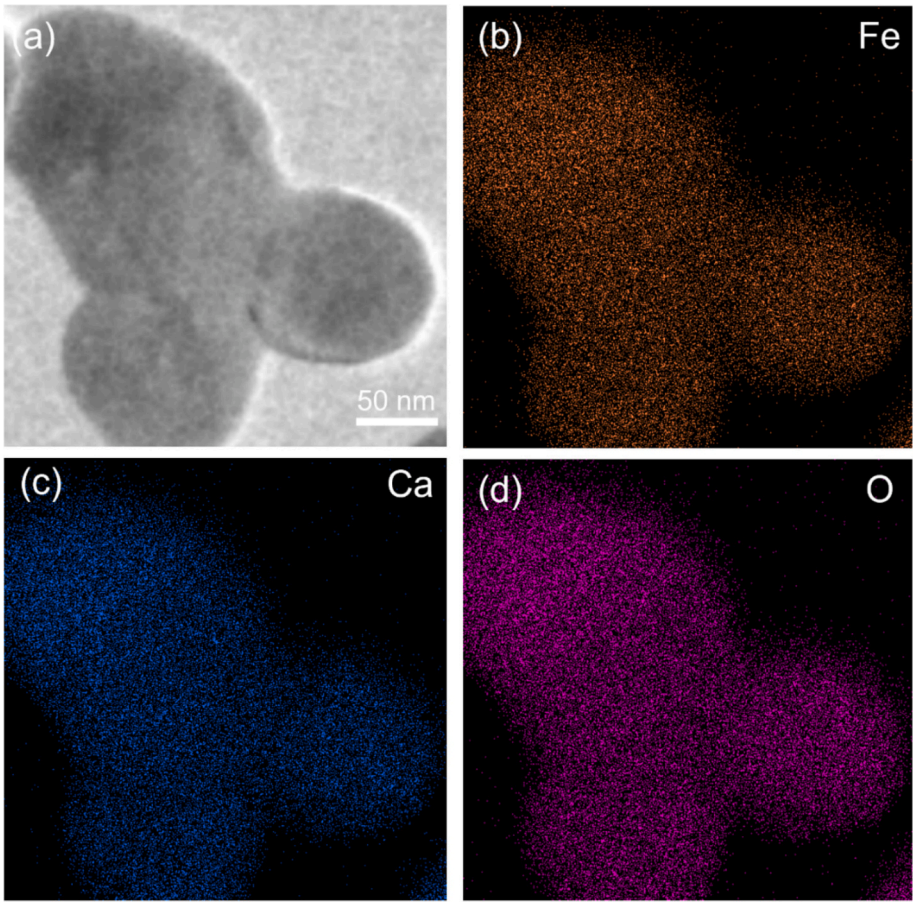

Fig. 8. (a) TEM image of $CaFe_2O_4/Ca_2Fe_2O_5$ composite fibers; EDS elemental mappings: (b) Fe, (c) Ca, and (d) O.

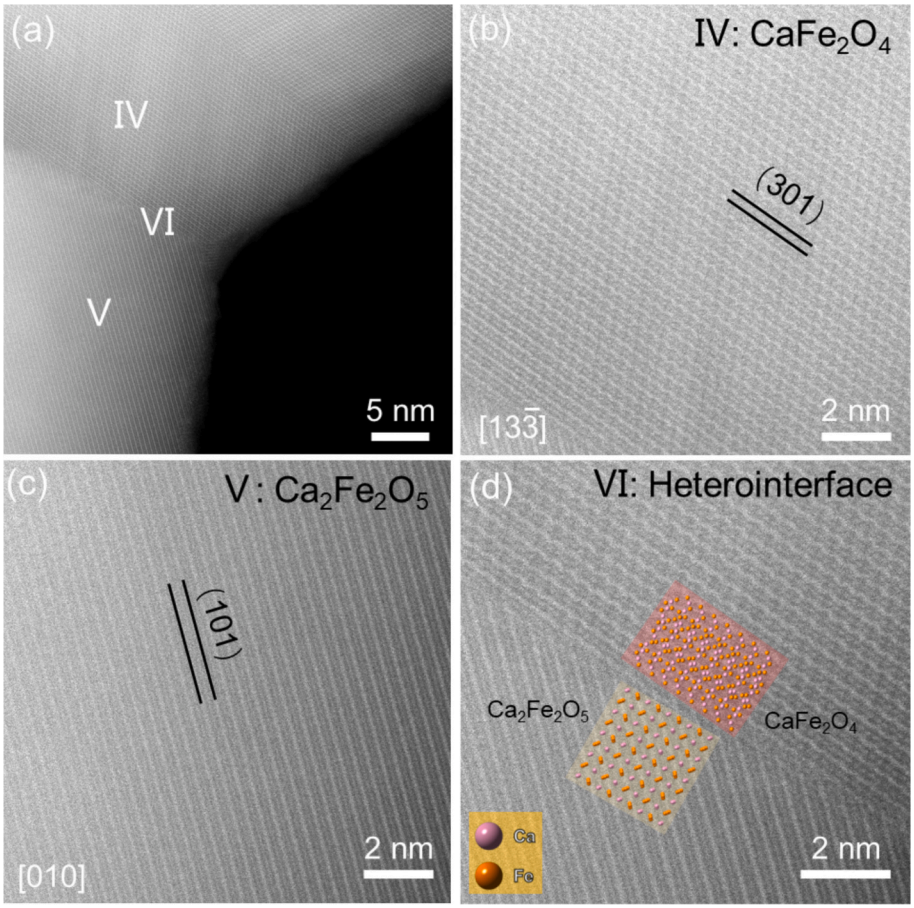

Fig. 9. HAADF images of the $CaFe_2O_4/Ca_2Fe_2O_5$ heterostructure interface. (a) HAADF image of the interface, (b) Enlarged HAADF image of grain IV, (c) Enlarged HAADF image of grain V, (d) Enlarged HAADF image of region VI, with an inset showing a schematic diagram of the atomic structures of $CaFe_2O_4/Ca_2Fe_2O_5$.

prioritized over high magnetic moment.

To demonstrate the influence of product morphology on the magnetic properties of ferrites, a comparison was conducted between previously-reported results and the experimental findings of this study. Damerio et al. [7] prepared $CaFe_2O_4$ thin film with a thickness of approximately 90 nm on TiO_2 substrates using pulsed laser deposition. The film exhibited a M_s of only 0.05 emu/g, which is significantly lower than that (0.19 emu/g) for the $CaFe_2O_4$ fibers in this work. Similarly, Phan et al. [44] prepared $Ca_2Fe_2O_5$ particles with diameters ranging from 2 to 10 μm via a solid-state method. These particles displayed distinct superparamagnetic characteristics with M_s of 0.13 emu/g, inferior to that of the $Ca_2Fe_2O_5$ fibers in this study. These comparisons suggest that, for both $CaFe_2O_4$ and $Ca_2Fe_2O_5$, the fiber morphology plays a substantial role in enhancing their magnetic properties. The enhancement of magnetic properties in submicron fibers compared to their bulk counterparts and thin films can be attributed to three primary factors [40]. Firstly, the one-dimensional structure of the submicron fibers exhibits pronounced shape anisotropy, facilitating the alignment of magnetic moments along the fiber axis. Secondly, the increased specific surface area of the fibers introduces a higher density of surface defects, which ultimately enhance the saturation magnetization. Thirdly, the smaller grain size within the fibers results in a greater number of grain boundaries and interfaces, generating stronger magnetic interactions compared to bulk particles and thin films.

To elucidate the mechanism by which the heterostructure interface enhances the magnetic properties of the as prepared ferrites, density functional theory (DFT) calculations of the magnetic structure and magnetic moments of $CaFe_2O_4$, $Ca_2Fe_2O_5$, and $CaFe_2O_4/Ca_2Fe_2O_5$ were performed. First, the spin-polarized states of $CaFe_2O_4$ and $Ca_2Fe_2O_5$ were calculated using first-principles calculations to determine their most stable spin structures, as shown in Figs. 11(a) and (b). The heterostructure interface was then constructed based on the most stable spin structures of $CaFe_2O_4$ and $Ca_2Fe_2O_5$, and the stable interface structure was calculated, as depicted in Fig. 11(c). Subsequently, the electronic density of states and magnetic moments of Fe atoms in the unit cells of three ferrites were computed. Fig. 11(d) presents the projected density of states (PDOS) for Fe atoms in the constructed unit cells of three ferrites.

As shown in Fig. 11(a), the Fe atoms in $CaFe_2O_4$ occupy octahedral sites but exhibit two distinct orientations, labeled as Fe1 and Fe2, with antiparallel magnetic moments. First-principles calculations yield magnetic moments of $-2.547\ \mu_B$ for Fe1 and $2.677\ \mu_B$ for Fe2, resulting in an average net magnetic moment of $0.065\ \mu_B$ (see Table 2). In Fig. 11(b), the Fe atoms in $Ca_2Fe_2O_5$ occupy both octahedral (Fe_{oct}) and tetrahedral (Fe_{tet}) sites, with their magnetic moments also aligned antiparallel. The calculated magnetic moments are $-3.003\ \mu_B$ for Fe_{oct} and $3.401\ \mu_B$ for Fe_{tet}, yielding an average net magnetic moment of $0.199\ \mu_B$. These results indicate that both the magnetic moments of Fe

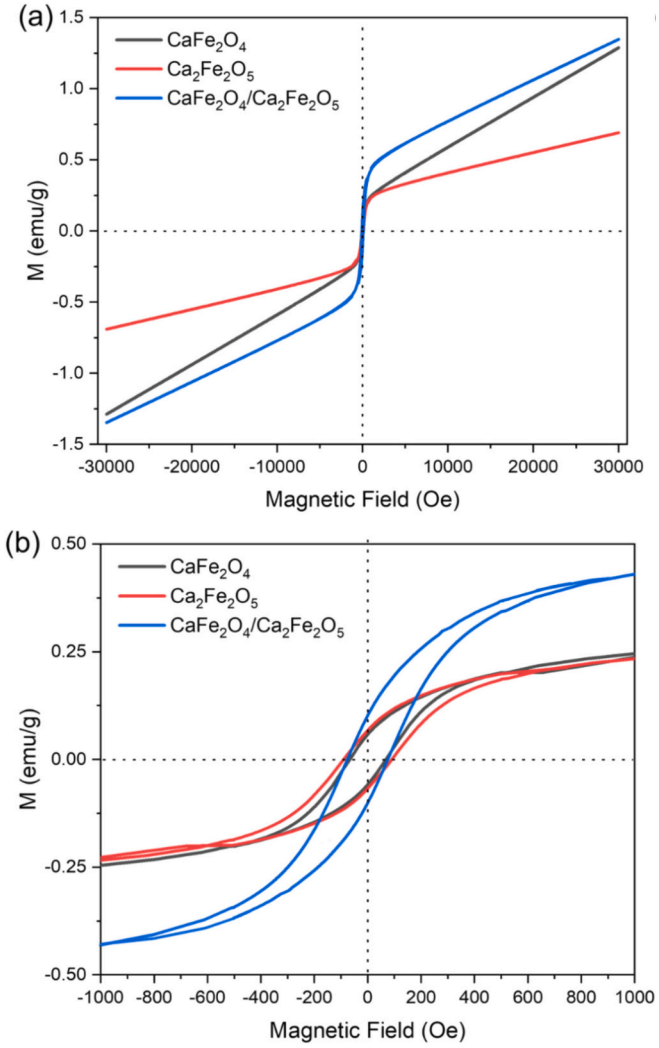

Fig. 10. (a) Magnetic hysteresis loops of $CaFe_2O_4$, $Ca_2Fe_2O_5$, and $CaFe_2O_4/Ca_2Fe_2O_5$ fibers measured at room temperature; (b) Magnified view near the zero-field region.

atoms and the average net magnetic moment in $Ca_2Fe_2O_5$ are higher than those in $CaFe_2O_4$. Notably, the average net magnetic moment of Fe atoms at the $CaFe_2O_4/Ca_2Fe_2O_5$ heterostructure interface is 0.280 μ_B, significantly higher than that of $CaFe_2O_4$ and $Ca_2Fe_2O_5$. The PDOS in Fig. 11(d) reveals that the presence of the interface alters the electronic structure distribution of Fe atoms. Specifically, the spin-down states of Fe1 in $CaFe_2O_4$ are significantly reduced at the interface, leading to a substantial increase in the net magnetic moment of Fe atoms. These findings suggest that the heterostructure interface modifies the crystal field environment of the original unit cells, enhancing the super-exchange interactions between Fe atoms, thereby improving the magnetic properties of ferrites.

4. Conclusions

In summary, three ferrite fibers of $CaFe_2O_4$, $Ca_2Fe_2O_5$ and $CaFe_2O_4/Ca_2Fe_2O_5$ have been fabricated via electrospinning and subsequent annealing. Extensive microstructure characterization confirms the formation of a well-defined heterointerface between the two orthorhombic phases of $CaFe_2O_4$ and $Ca_2Fe_2O_5$. Hysteresis loop measurements demonstrate that the $CaFe_2O_4/Ca_2Fe_2O_5$ composite fibers possess enhanced magnetic properties compared to their single-phase counterparts. First-principles calculations reveal that the interfacial region provides a distinct local environment that strengthens Fe-O-Fe super-exchange interactions, thereby leading to improved magnetization. This work not only presents a feasible interface-engineering strategy for enhancing the magnetic performance of Ca-based ferrites but also offers fundamental insight into the role of heterointerfaces in modulating magnetic behavior, which may guide the design of advanced ferrite materials for magnetic and multifunctional applications.

CRediT authorship contribution statement

Zhibin Ling: Writing – original draft, Resources, Investigation, Formal analysis, Data curation, Conceptualization. **Feiyu Diao:** Writing – review & editing, Supervision, Resources. **Fei Xie:** Resources, Investigation. **Rongsheng Cai:** Validation, Data curation. **Xuyan Xue:** Supervision, Software. **Yiqian Wang:** Writing – review & editing, Supervision, Funding acquisition, Conceptualization.

Declaration of competing interest

The authors declare that they have no known competing financial interests or personal relationships that could have appeared to influence the work reported in this paper.

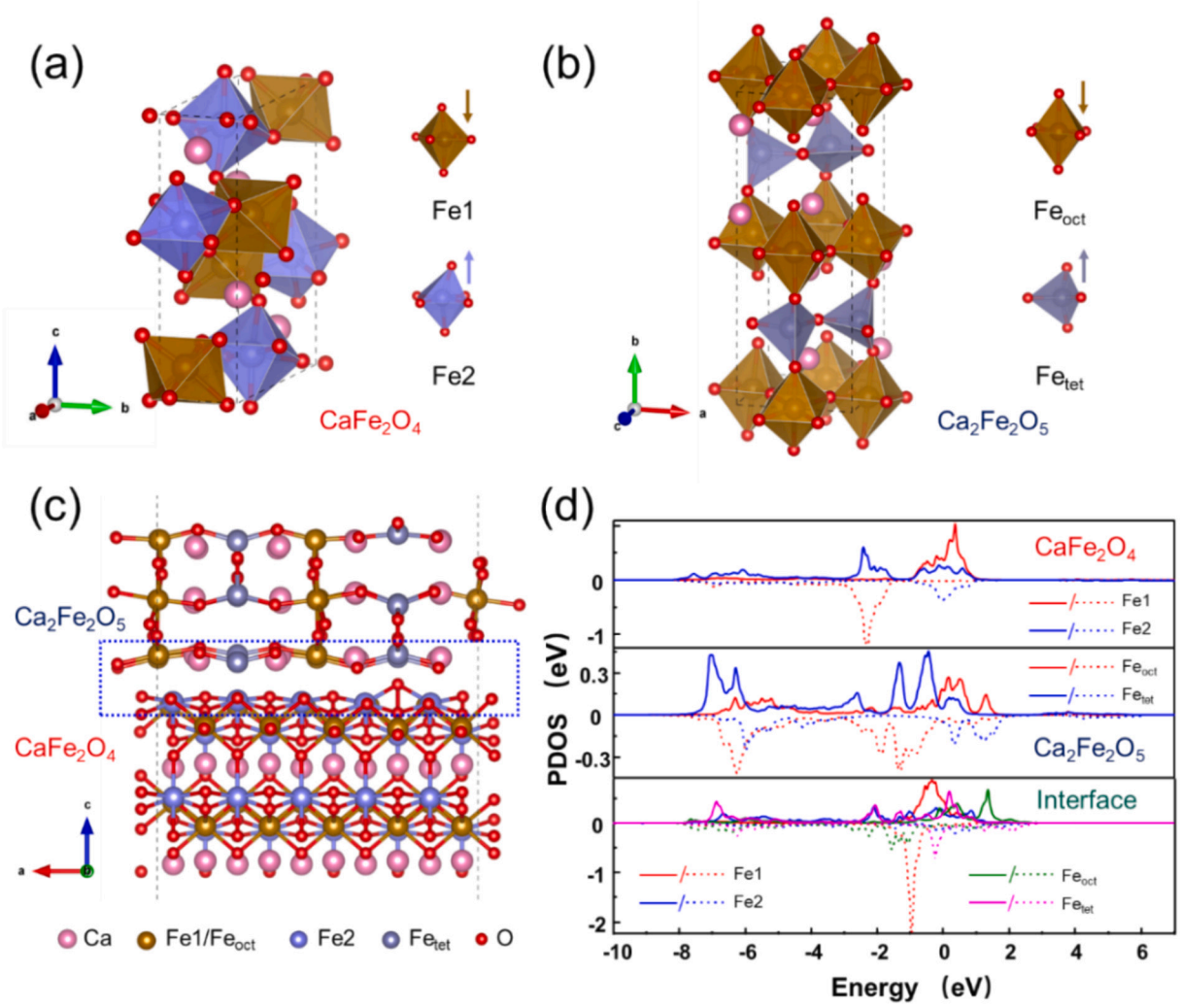

Fig. 11. (a) Unit cell of $CaFe_2O_4$; (b) Unit cell of $Ca_2Fe_2O_5$; (c) Schematic illustration of the $CaFe_2O_4/Ca_2Fe_2O_5$ heterointerface structure; (d) PDOS of Fe atoms in $CaFe_2O_4$, $Ca_2Fe_2O_5$, and at the $CaFe_2O_4/Ca_2Fe_2O_5$ heterointerface.

Table 2
Magnetic moments of Fe atoms in the unit cell of $CaFe_2O_4$, $Ca_2Fe_2O_5$, and at the $CaFe_2O_4/Ca_2Fe_2O_5$ heterointerface.

Material	Atom	M(μ_B)	Average M(μ_B)
$CaFe_2O_4$	Fe1	−2.547	0.065
	Fe2	2.677	
$Ca_2Fe_2O_5$	Fe_{oct}	−3.003	0.199
	Fe_{tet}	3.401	
$CaFe_2O_4/Ca_2Fe_2O_5$	Fe1	−1.372	0.280
	Fe2	2.274	
	Fe_{oct}	−2.209	
	Fe_{tet}	2.427	

Acknowledgments

The authors gratefully acknowledge the financial support from the High-end Foreign Experts Programs of the Ministry of Science and Technology, China (Grant Nos.: G2022025015L, G2022025016L, H20250033), and Shandong Province "Double-Hundred Talent Plan" Program (Grant No.: WST2018006). Y. Q. Wang acknowledges the support from the Taishan Scholar Program of Shandong Province, China, the Qingdao International Center of Semiconductor Photoelectric Nanomaterials, and the Shandong Provincial University Key Laboratory of Optoelectrical Material Physics and Devices.

Data availability

Data will be made available on request.

References

[1] R. Jasrotia, J. Prakash, Y.B. Saddeek, A.H. Alluhayb, A.M. Younis, N. Lakshmaiya, C. Prakash, K. Aly, M. Sillanpää, Y.A. Ismail, Cobalt ferrites: structural insights with potential applications in magnetics, dielectrics, and catalysis, Coord. Chem. Rev. 522 (2025) 216198.
[2] R. Jasrotia, K. Raj, M. Ramya, R. Kumar, D. Pathania, Y. Kumar, A. Kandwal, Magnesium ferrites and their composites based photocatalysts: synthesis approaches, effect of doping, and operational parameters on photocatalytic performance for wastewater remediation, J. Magnesium Alloys 12 (2024) 3996–4044.
[3] X. Han, B. Duan, L. Liu, S. Fang, W. Wang, Preparation and applications of calcium ferrite as a functional material: a review, Int. J. Miner. Metall. Mater. 32 (2025) 292–310.
[4] B. Xue, J. Luo, F. Zhang, Z. Fang, Biodiesel production from soybean and Jatropha oils by magnetic $CaFe_2O_4$–$Ca_2Fe_2O_5$-based catalyst, Energy 68 (2014) 584–591.
[5] A. Mukhopadhyay, M. Paul, A. Bhattacharya, I. Das, Role of A site and B site ion substitutions on the low-temperature magnetic behaviour of $Ca_2Fe_2O_5$, J. Magn. Magn. Mater. 588 (2023) 171457.
[6] A. Kumar Das, A. Srinivasan, Structural transition and associated magnetic properties of heat treated electrospun one-dimensional $CaFe_2O_4$, Chem. Phys. Lett. 786 (2022) 139169.
[7] S. Damerio, P. Nukala, J. Juraszek, P. Reith, H. Hilgenkamp, B. Noheda, Structure and magnetic properties of epitaxial $CaFe_2O_4$ thin films, npj Quant. Mater. 5 (2020) 33.

[8] Y.H. Chang, W.C. Tseng, C.C. Kaun, Y.H. Su, J.J. Wu, $Mg_2Fe_2O_5$ nanoparticle-decorated $Ca_2Fe_2O_5$–$CaFe_2O_4$ heterostructure for efficient photocatalytic CO_2 conversion, ACS Sustain. Chem. Eng. 10 (2022) 12651–12658.

[9] G.P. Wheeler, K.S. Choi, Investigation of p-type $Ca_2Fe_2O_5$ as a photocathode for use in a water splitting photoelectrochemical cell, ACS Appl. Energy Mater. 1 (2018) 4917–4923.

[10] H.G. Kim, P.H. Borse, J.S. Jang, E.D. Jeong, O.S. Jung, Y.J. Suh, J.S. Lee, Fabrication of $CaFe_2O_4$/$MgFe_2O_4$ bulk heterojunction for enhanced visible light photocatalysis, Chem. Commun. 45 (2009) 5889–5891.

[11] A. Šutka, M. Kodu, R. Pärna, R. Saar, I. Juhnevica, R. Jaaniso, V. Kisand, Orthorhombic $CaFe_2O_4$: a promising p-type gas sensor, Sensors Actuators B Chem. 224 (2016) 260–265.

[12] M. Naseri, E. Naderi, A.R. Sadrolhosseini, Effect of phase transformation on physical and biological properties of PVA/$CaFe_2O_4$ nanocomposite, Fibers Polym. 17 (2016) 1667–1674.

[13] A. El-Rafei, A.S. El-Kalliny, T.A. Gad-Allah, Electrospun magnetically separable calcium ferrite nanofibers for photocatalytic water purification, J. Magn. Magn. Mater. 428 (2017) 92–98.

[14] G. Lal, K. Punia, S.N. Dolia, P. Alvi, S. Dalela, S. Kumar, Rietveld refinement, Raman, optical, dielectric, Mössbauer and magnetic characterization of superparamagnetic fcc-$CaFe_2O_4$ nanoparticles, Ceram. Int. 45 (2019) 5837–5847.

[15] C.B. Azzoni, M.C. Mozzati, V. Massarotti, D. Capsoni, M. Bini, New insights into the magnetic properties of the $Ca_2Fe_2O_5$ ferrite, Solid State Sci. 9 (2007) 515–520.

[16] X. Bo, D. Wang, X. Wan, Calculated magnetic exchange interactions in brownmillerite $Ca_2Fe_2O_5$, Phys. Lett. A 394 (2021) 127202.

[17] A. Manohar, V. Vijayakanth, N. Mameda, K.S. Ganesh, K.H. Kim, Revolutionizing nanoscience: exploring the multifaceted applications and cutting-edge advancements in spinel $CaFe_2O_4$ nanoparticles – a review, Inorg. Chem. Commun. 161 (2024) 111999.

[18] S. Thundiyil, C. Vinod, S. Kurungot, R.N. Devi, Role of B site ions in bifunctional oxygen electrocatalysis: a structure–property correlation study on doped $Ca_2Fe_2O_5$ brownmillerites, Phys. Chem. Chem. Phys. 22 (2020) 15520–15527.

[19] H.A. Raza, I. Karakaya, O. Dag, Nanoarchitectonics of mesoporous $CaFe_2O_4$ thin-film electrodes from salt-surfactant lyotropic liquid crystalline mesophases and their OER performance, ACS Appl. Energy Mater. 6 (2023) 9681–9697.

[20] W. Guo, L. Huang, X. Liu, J. Wang, J. Zhang, Enhanced isoprene gas sensing performance based on p-$CaFe_2O_4$/n-$ZnFe_2O_4$ heterojunction composites, Sensors Actuators B Chem. 354 (2022) 131243.

[21] W. Li, Q. Song, M. Li, Y. Yuan, J. Zhang, N. Wang, Z. Yang, J. Huang, J. Lu, X. Li, Chemical heterointerface engineering on hybrid electrode materials for electrochemical energy storage, Small Methods 5 (2021) 2100444.

[22] C. Wang, H. Shang, Y. Wang, H. Xu, J. Li, Y. Du, Interfacial electronic structure modulation enables $CoMoO_x$/CoO_x/RuO_x to boost advanced oxygen evolution electrocatalysis, J. Mater. Chem. A 9 (2021) 14601–14606.

[23] J. Chureemart, S. Boonchui, R. Chantrell, P. Chureemart, Current-induced domain wall motion: comparison of STT and SHE, J. Magn. Magn. Mater. 529 (2021) 167838.

[24] D. Luo, Y. Kang, Synthesis and characterization of novel $CaFe_2O_4$/Bi_2O_3 composite photocatalysts, Mater. Lett. 225 (2018) 17–20.

[25] F. Xie, M. Sun, X. Sheng, Q. Zhang, Z. Ling, S. Hao, F. Diao, Y. Wang, Graphene-wrapped Fe_2TiO_5 nanoparticles with enhanced performance as lithium-ion battery anode, Mater. Lett. 358 (2024) 135877.

[26] F. Xie, X. Sheng, Z. Ling, S. Hao, Q. Zhang, M. Sun, G. Liu, F. Diao, Y. Wang, Flexible electrospun iron/manganese-based compounds/carbon fibers: phase transformation and electrochemical properties, Electrochim. Acta 470 (2023) 143288.

[27] X. Sheng, T. Li, M. Sun, G. Liu, Q. Zhang, Z. Ling, S. Gao, F. Diao, J. Zhang, F. Rosei, Flexible electrospun iron compounds/carbon fibers: phase transformation and electrochemical properties, Electrochim. Acta 407 (2022) 139892.

[28] G. Kresse, J. Furthmüller, Efficient iterative schemes for ab initio total-energy calculations using a plane-wave basis set, Phys. Rev. B 54 (1996) 11169.

[29] J.P. Perdew, K. Burke, M. Ernzerhof, Generalized gradient approximation made simple, Phys. Rev. Lett. 77 (1996) 3865.

[30] J. Wang, X. Xue, Y. Wang, Tuning the structural and magnetic properties of electrospun strontium-iron-oxide nanofibers with different stoichiometry, Mater. Charact. 200 (2023) 112884.

[31] L. Zhang, F. Xie, S. Hao, F. Diao, Y. Wang, Annealing condition engineering of electrospun iron-titanium oxide nanofibers for enhanced lithium storage performance, Electrochim. Acta 536 (2025) 146746.

[32] S. Hao, B. Zhang, Q. Zhang, M. Sun, R. Cai, F. Diao, Y. Wang, Effectiveness of three distinct strategies of constructing ZnO-based composites for enhanced electrochemical performance, J. Phys. Chem. Solids 211 (2026) 113502.

[33] M. Sun, G. Liu, S. Hao, F. Diao, F. Rosei, R. Cai, Y. Wang, Correlation between spinel structure and electrochemical kinetic behavior of spinel ferrites, J. Electroanal. Chem. 1005 (2026) 119870.

[34] B. Zhang, F. Xie, S. Hao, M. Sun, F. Diao, R. Cai, Y. Wang, Effect of annealing atmosphere on the phase composition and electrochemical properties of iron-oxide-based electrospun nanofibers, J. Energy Storage 124 (2025) 116851.

[35] J. Wang, X. Sheng, S. Hao, G. Liu, R. Cai, X. Xue, Y. Wang, Construction of $Fe_{0.64}Ni_{0.36}$@graphite nanoparticles via corrosion-like transformation from $NiFe_2O_4$ and surface graphitization in flexible carbon nanofibers to achieve strong wideband microwave absorption, J. Colloid Interface Sci. 657 (2024) 193–207.

[36] A. Behera, D. Kandi, S. Sahoo, K. Parida, Construction of isoenergetic band alignment between CdS QDs and $CaFe_2O_4$@$ZnFe_2O_4$ heterojunction: a promising ternary hybrid toward norfloxacin degradation and H_2 energy production, J. Phys. Chem. C 123 (2019) 17112–17126.

[37] A.K. Das, R. Govindaraj, A. Srinivasan, Structural and magnetic properties of sol-gel derived $CaFe_2O_4$ nanoparticles, J. Magn. Magn. Mater. 451 (2018) 526–531.

[38] X. Huang, J. Zhang, S. Xiao, T. Sang, G. Chen, Unique electromagnetic properties of the zinc ferrite nanofiber, Mater. Lett. 124 (2014) 126–128.

[39] R. Araujo, E. Nascimento, H. Sales, M. Silva, G. Neves, R. Menezes, $CaFe_2O_4$ ferrite nanofibers *via* solution blow spinning (SBS), Cerâmica 66 (2020) 467–473.

[40] M. Tiwari, N. Bangruwa, D. Mishra, 0D, 1D, and 2D magnetic nanostructures: classification and their applications in modern biosensors, Talanta Open 8 (2023) 100257.

[41] M. Shokouhimehr, Y.Z. Piao, J. Kim, Y.J. Jang, T. Hyeon, A magnetically recyclable nanocomposite catalyst for olefin epoxidation, Angew. Chem. Int. Ed. 46 (2007) 7039–7043.

[42] Y. Qian, X.F. Meng, H.J. Liu, X.Y. Wang, Y.F. Lin, X.Y. Shi, Z.G. Sheng, H. Wang, Magnetic field-induced synthesis of one-dimensional nickel nanowires for enhanced microwave absorption, Adv. Mater. Interfaces 10 (2023) 2201604.

[43] C. Massner, F. Sigmund, S. Pettinger, M. Seeger, C. Hartmann, N.P. Ivleva, R. Niessner, H. Fuchs, M.H. de Angelis, A. Stelzl, N.L. Koonakampully, H. Rolbieski, U. Wiedwald, M. Spasova, W. Wurst, V. Ntziachristos, M. Winklhofer, G. G. Westmeyer, Genetically controlled lysosomal entrapment of superparamagnetic ferritin for multimodal and multiscale imaging and actuation with low tissue attenuation, Adv. Funct. Mater. 28 (2018) 1706793.

[44] T.L. Phan, N. Tran, D.H. Kim, P.T. Tho, B.T. Huy, T.N. Dang, D.S. Yang, B. Lee, Electronic structure and magnetic properties of Al-doped $Ca_2Fe_2O_5$ brownmillerite compounds, J. Am. Ceram. Soc. 101 (2018) 2181–2189.